Localization of vibrational modes leads to reduced thermal conductivity of amorphous heterostructures

Ashutosh Giri,[1,*] Brian F. Donovan,[2] and Patrick E. Hopkins[1,3,4,†]
[1]*Department of Mechanical and Aerospace Engineering, University of Virginia, Charlottesville, Virginia 22904, USA*
[2]*Department of Physics, United States Naval Academy, Annapolis, Maryland 21042, USA*
[3]*Department of Materials Science and Engineering, University of Virginia, Charlottesville, Virginia 22904, USA*
[4]*Department of Physics, University of Virginia, Charlottesville, Virginia 22904, USA*

(Received 12 February 2018; revised manuscript received 24 April 2018; published 24 May 2018)

We investigate the vibrational heat transfer mechanisms in amorphous Stillinger-Weber silicon and germanium-based alloys and heterostructures via equilibrium and nonequilibrium molecular dynamics simulations along with lattice dynamics calculations. We find that similar to crystalline alloys, amorphous alloys demonstrate large size effects in thermal conductivity, while layering the constituent materials into superlattice structures leads to length-independent thermal conductivities. The thermal conductivity of an amorphous Si_xGe_{1-x} alloy reduces by as much as ∼53% compared to the thermal conductivity of amorphous silicon; compared to the larger reduction in crystalline phases due to alloying, we show that compositional disorder rather than structural disorder has a larger impact on the thermal conductivity reduction. Our thermal conductivity predictions for a-Si/a-Ge superlattices suggest that the alloy limit in amorphous SiGe-based structures can be surpassed with interface densities above $\sim 0.35\ nm^{-1}$. We attribute the larger reduction in thermal conductivity of layered Si/Ge heterostructures to greater localization of modes at and around the cutoff frequency of the softer layer as demonstrated via lattice dynamics calculations and diffusivities of individual eigenmodes calculated according to the Allen-Feldman theory [P. B. Allen and J. L. Feldman, Phys. Rev. B **48**, 12581 (1993)] for our amorphous SiGe-based alloys and superlattice structures.

DOI: 10.1103/PhysRevMaterials.2.056002

I. INTRODUCTION

Usually in homogeneous crystalline solids, thermal transport is adequately described by the phonon gas model in which heat propagates through the collective oscillation of atoms as plane waves with well-defined phase and group velocities [1–4]. The seminal work of Allen and Feldman challenged this notion and the general applicability of the phonon gas model in describing thermal transport across systems that lack periodicity, i.e., for disordered and amorphous materials [5,6]. The discrepancy between the conceptual description governing the phonon gas model and the harmonic coupling of delocalized and nonpropagating modes in amorphous solids prompted them to introduce a new taxonomy for describing vibrational modes. These are classified as propagons that are delocalized (and propagating), diffusons that are delocalized (and nonpropagating), and locons that are localized (and nonpropagating) [5–8]. In their theoretical description (denoted by AF theory herein), diffusons mediate heat through harmonic coupling while locons do not contribute to the thermal conductivity directly in the harmonic approximation.

The contributions from these various modes to the thermal conductivity were further demonstrated by Larkin and McGaughey through normal-mode decomposition analysis and Green-Kubo (GK) simulations, showing that propagons in amorphous silicon contribute substantially to the overall thermal conductivity even though these modes make up a small percentage of the vibrational density of states (DOS) [9]. Recently, we have also shown experimentally that size effects are prominent for amorphous Si thin films thicker than ∼100 nm, suggesting that propagating modes with plane wave characteristics can substantially increase the thermal conductivity of these material systems [10]. In this context, nanostructures such as nanowires and superlattices (SLs) with characteristic dimensions smaller than the mean-free paths of these propagating modes have been shown to significantly lower the observed thermal conductivities of amorphous silicon-based materials [11,12].

For interfaces between dissimilar crystalline solids, it is well known that phonons readily scatter at these boundaries and impose a thermal resistance, which is generally determined from the differences in densities, structures, and stiffnesses of the constituent solids [13,14]. Therefore, crystalline SLs with high interface densities can exhibit thermal conductivities lower than those of their constituent components through incoherent scattering of phonons in either material with mean-free paths smaller than the thicknesses of the constituent materials [15–24]. This approach to thermal conductivity reduction can lead to the design of crystalline SLs with thermal conductivities below their corresponding alloy limit [22,24,25]. In this regard, while SL structures specifically target the scattering of lower-frequency phonons, higher-frequency vibrations are scattered due to impurities in alloys, which leads to large size effects in their observed thermal conductivities due to pronounced

*ag4ar@virginia.edu
†phopkins@virginia.edu

contribution of low-frequency phonons that dictate heat transport [26,27]. On the other hand, for amorphous materials where diffusons can largely dictate the thermal conductivity [28–31], it is still unclear what roles interfaces or impurity disorder have on the overall thermal transport. Moreover, if locons do not contribute to thermal conductivity in a harmonic solid, can these vibrational modes be manipulated in order to lower the overall thermal conductivity of amorphous materials?

So far, crystalline alloys and SLs have been studied extensively; however, a systematic study investigating the underlying mechanisms responsible for dictating thermal transport in amorphous alloys and superlattices is still lacking and could potentially answer some of the questions posed above. Therefore, in the present work, we study the mechanisms affecting thermal transport in Si- and Ge-based amorphous superlattices and the random alloy counterparts of the constituent materials. For this purpose, we use a combination of lattice dynamics calculations, nonequilibrium molecular dynamics simulations (NEMD), and the Green-Kubo (GK) formalism under the equilibrium MD simulations framework to understand the heat transport mechanisms in amorphous alloys and superlattices. Note that in our simulations described in this work, we use the Stillinger-Weber potential to describe the silicon and germanium interatomic forces [32,33], as described in Sec. II. Thus, it is important to note that the Si- and Ge-based structures simulated in this work are "Stillinger-Weber" silicon-germanium. For the sake of brevity, we omit the "Stillinger-Weber" descriptor when referring to the various materials that we investigate in this work.

We find that similar to crystalline alloys, amorphous alloys demonstrate large size effects in thermal conductivity, while layering the constituent materials in SL structures leads to size-independent thermal conductivities. In comparison to crystalline $Si_{0.5}Ge_{0.5}$ alloys with ∼95% reduction in thermal conductivity (with respect to the thermal conductivity of crystalline Si, as reported in Ref. [27] via first-principles calculations), a-$Si_{0.5}Ge_{0.5}$ alloys demonstrate a ∼53% reduction in thermal conductivity compared to that of a-Si. However our thermal conductivity predictions for a-Si/a-Ge SLs suggest that this alloy limit can be surpassed with interface densities above ∼0.35 nm^{-1}. By calculating the inverse participation ratios (IPRs) and diffusivities according to the AF theory for individual eigenmodes in the alloys and SLs, we attribute the larger reduction in thermal conductivity of SL structures to greater localization of modes at and around the cutoff frequency of the softer layer in comparison to the disordered alloy counterparts. We utilize this approach to reducing the thermal conductivity in layered materials by constructing amorphous SLs that demonstrate large reductions in diffusivities for certain eigenmodes in the spectrum as described in the Appendix. Doing so leads to higher anisotropies in thermal conductivity of silicon-based amorphous SL structures.

II. METHODOLOGY

Our amorphous structures were created using the melt-quench technique [35], and the subsequent MD simulations were performed via the LAMMPS package with a 0.5 fs time step throughout all simulations [36]. Starting with a diamond cubic lattice, we heat the domains at a temperature of 8000 K until the atoms lose memory of their initial positions. Rapid quenching is then applied to cool the systems at a constant volume followed by annealing the systems at 1100 K for a total of 10 ns to remove metastabilities as evidenced from the plateau of the potential energy for systems during this process [9,37]. The systems were then equilibrated at 500 K for a total of 1 ns under the isothermal-isobaric ensemble with the number of particles, pressure, and temperature of the system held constant at 0 bar pressure. Throughout the equilibration process, periodic boundary conditions were applied in all three principal directions and atomic densities and atomic coordinations were monitored to ensure no voids were formed. Our SL structures were initially prepared from a single species with the melt-quench technique described above. Depending on the position in the computational cell, the atoms are then varied in order to create layered SL structures. Examples of the computational domains for our a-$Si_{0.5}Ge_{0.5}$ alloy and a-Si/a-Ge SL are shown in Fig. 1(a). To determine the thermal conductivities, NEMD and/or GK frameworks were implemented on the equilibrated structures. The main purpose for using NEMD simulations is to highlight size effects or the lack thereof in thermal conductivity predictions for the different systems studied in this work. The GK approach is used as a check to ensure convergent results for our NEMD predictions, and also due to the fact that in comparison to NEMD simulations, GK simulations require smaller domain sizes for accurate predictions of thermal conductivities [38], which can substantially lower the computational costs. Furthermore, GK simulations also provide the capability of simultaneously calculating the thermal conductivities in the in-plane and cross-plane directions, which will be useful in predicting the anisotropy in thermal conductivity for our SL structures.

For the NEMD simulations, a steady-state temperature gradient was established by creating a fixed wall at either side of the domain (in the z direction) and adding a fixed amount of energy per time step to a heat bath at one end of the computational domain, while removing an equal amount of heat from a cold bath at the other end of the domain. Depending on the length of the domain, energy is added and removed at a specified rate (for example, energy is added and removed at a rate of 0.25 eV ps^{-1} for the shortest domain length of 16 nm) under the microcanonical ensemble where the number of atoms (N), volume (V), and energy (E) of the system are held constant. For all NEMD simulations, the cross sections of the computational domains are set to $10a_0 \times 10a_0$ with a_0 specified by the silicon lattice constant of 5.43 Å. The temperature profile along the z direction is obtained by averaging the temperature of the atoms along equally spaced bins in the applied heat flux direction for a total of 10 ns. As the systems take time to reach steady state, the initial 3 ns of data are ignored to create time-averaged steady-state temperature profiles from which the thermal conductivity for our structures is calculated via Fourier's law. As domain lengths can have a significant influence on the predicted thermal conductivity [38], we calculate thermal conductivities for different domain lengths to accurately predict the thermal conductivity for a bulk system. For this purpose, the inverse of thermal conductivity, $1/\kappa$, vs the inverse of the computational domain length, $1/d$, which shows a linear trend, is extrapolated to $1/d = 0$ [39]. This approach has been used to predict

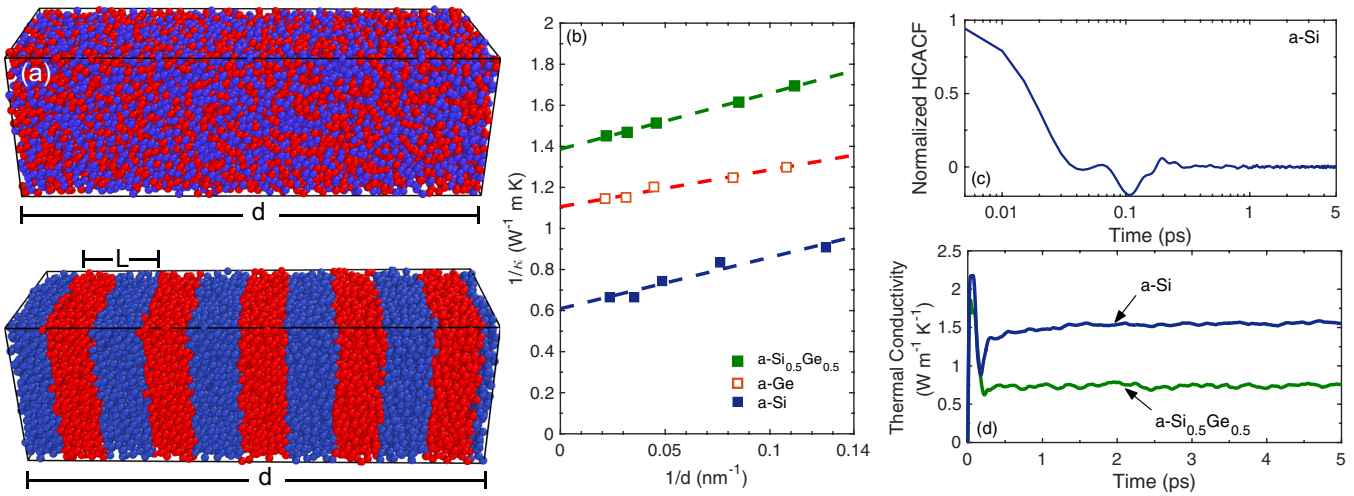

FIG. 1. (a) Schematics of the $55 \times 55 \times 160$ Å^3 computational domains for an a-$Si_{0.5}Ge_{0.5}$ structure (top panel) and an a-Si/a-Ge superlattice with an interface density of 0.64 nm^{-1} (bottom panel). (b) NEMD-predicted inverse of size-dependent thermal conductivities vs inverse of the computational domain length in the applied heat flux direction for a-Si (hollow blue squares), a-Ge (hollow red squares), and a-$Si_{0.5}Ge_{0.5}$ (solid green squares). The linear dependence of the MD results suggests that pronounced size effects are observed in the apparent thermal conductivities. The extrapolation of the linear fits to $1/d \to 0$ predicts the thermal conductivity of an infinite system, assuming that the minimum system size used in these NEMD simulations is comparable to or larger than the largest mean-free paths of the delocalized modes that dominate the thermal transport in these amorphous systems [34]. (c) Heat current autocorrelation function (HCACF) vs time for a-Si, which shows that the HCACF decays to zero within a picosecond. (d) Converged value of the thermal conductivity obtained from the integral of the HCACF for a-$Si_{0.5}Ge_{0.5}$ and a-Si at 300 K.

convergent values of thermal conductivities of infinite systems for different materials [38–42]. Figure 1(b) shows examples of this approach to calculate the thermal conductivity of a-Si, a-Ge, and a-$Si_{0.5}Ge_{0.5}$, which agree very well with predictions from our GK approach (as explained in detail below), as well as with previously reported values for a-Si and a-Ge. This suggests that the extrapolation method used in our NEMD simulations is valid for our SW-based systems as the minimum system size used is comparable to or larger than the largest mean-free paths of the delocalized modes that dominate thermal transport in these amorphous systems [34].

The GK method under the equilibrium MD simulation framework has been utilized to predict the thermal conductivity of crystalline and amorphous systems alike [43–46]. In this method, the thermal conductivity in the αth direction (either in-plane or out-of-plane) is given by

$$\kappa_\alpha = \frac{1}{k_B V T^2} \int_0^\infty \langle S_\alpha(t) S_\alpha(0) \rangle dt, \qquad (1)$$

where t is the time, T and V are the temperature and volume of the system under consideration, respectively, and $\langle S_\alpha(t) S_\alpha(0) \rangle$ is the αth component of the heat current autocorrelation function (HCACF). All the GK thermal conductivity predictions are carried out under the *NVE* ensemble for a total of 10 ns. The heat current is calculated every 10 time steps during the data collection period and the integration is carried out until the HCACF completely decays to zero. An example of the calculated HCACF as a function of time for a-$Si_{0.5}Ge_{0.5}$ is shown in Fig. 1(c) where the HCACF decays to zero by the first picosecond. The corresponding thermal conductivity calculation from the integral of the HCACF is shown in Fig. 1(d), where the data are averaged from 2 to 5 picoseconds to accurately predict the thermal conductivity of the various systems. For comparison, we also include the thermal conductivity calculated for a-Si from the corresponding integral of the HCACF. As domain sizes can alter the calculated thermal conductivities even under equilibrium MD simulations if all the available vibrational modes are not included in the simulation cell [9], we check for computational domain size effects by conducting GK simulations on domain sizes of $55 \times 55 \times 55$ Å^3 and $92 \times 92 \times 92$ Å^3. The GK predictions for these two domain sizes with 8000 and 39 304 atoms produce statistically invariant thermal conductivities of 1.51 ± 0.13 W m^{-1} K^{-1} and 1.55 ± 0.16 W m^{-1} K^{-1}, respectively. To assess statistical uncertainties for our MD-predicted thermal conductivities, we perform 3 to 5 different simulations with varying initial conditions for our NEMD and EMD simulations, respectively.

III. RESULTS AND DISCUSSION

A. Thermal conductivity of amorphous SiGe alloys and superlattices

Figure 2(a) shows the thermal conductivities of a-Si, a-Ge, and the a-Si_xGe_{1-x} alloys (red squares) as a function of alloy concentration calculated via the NEMD approach, which extrapolates to an infinite domain size from results for computational domain lengths ranging from 9 to 45 nm. As stated earlier, smaller domain lengths in general can significantly reduce the observed thermal conductivity since modes with long mean-free paths can scatter at the domain boundaries and heat baths. The linear dependence of $1/\kappa$ vs $1/d$ as shown in Fig. 1(b) suggests that propagating modes contribute considerably to the thermal conductivities of a-Si, a-Ge, and their alloys. This is in line with the recent results from He *et al.* [42] and Larkin *et al.* [47] where they have shown that a significant

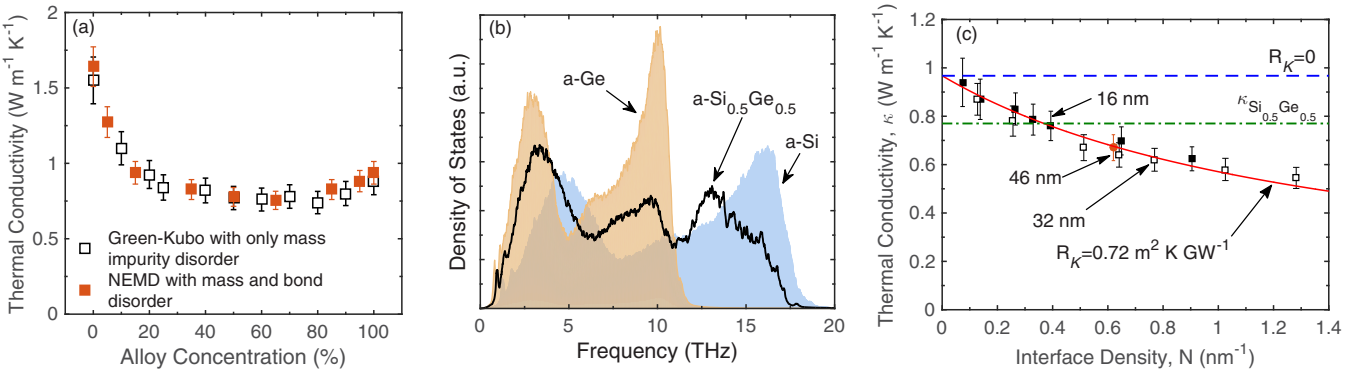

FIG. 2. (a) Thermal conductivity as a function of alloy concentration for a-Si$_x$Ge$_{1-x}$. The solid squares represent simulations with differences in the MD potential for Si-Si, Si-Ge, and Ge-Ge bonds, whereas the hollow squares represent simulations with only mass mismatch between silicon and germanium atoms in the alloys. The agreement between the two sets of data suggests that mass disorder controls thermal conductivity in amorphous SiGe alloys. (b) Vibrational density of states for a-Si, a-Ge, and a-Si$_{0.5}$Ge$_{0.5}$. (c) NEMD-predicted thermal conductivities of amorphous Si/Ge superlattices plotted as a function of interface densities. Hollow square symbols are data from simulations with domain size of 16 nm, solid square symbols are data with a domain size of 32 nm, and solid circle symbol is the data for a domain size of 46 nm. The agreement between the data for all three domain sizes suggests that size effects and, therefore, propagating modes in the amorphous superlattice Si/Ge structures do not significantly affect the thermal conductivity, which is in contrast to the results for the homogeneous a-Si, a-Ge, and a-Si$_x$Ge$_{1-x}$ structures. A thermal circuit model predicts a very high conductance (low resistance, R_K) across an individual a-Si/a-Ge interface, shown by the red solid line. For comparison, the thermal conductivity of our a-Si$_{0.5}$Ge$_{0.5}$ is shown by the dash-dotted line.

portion of the thermal conductivity in a-Si is due to vibrations that are propagating and delocalized modes (propagons). The NEMD-predicted thermal conductivities for our a-Si and a-Ge are 1.50 ± 0.13 and 0.94 ± 0.08 W m^{-1} K^{-1}, respectively, which are consistent with previous results [48,49]. The effect of alloying is seen to reduce the thermal conductivities by as much as ∼53% relative to the thermal conductivity of a-Si [Fig. 2(a)]. It is also interesting to note that the decrease in thermal conductivity to the minimum value achievable in this binary system occurs at ∼25% germanium concentration, while in crystalline Si$_x$Ge$_{1-x}$ alloys, the drop in thermal conductivity is much more drastic with the minimum realized at almost ∼12% Ge concentration [50]; similar results are obtained for crystalline SiGe alloys from density functional theory calculations [27]. Furthermore, crystalline Si$_{0.5}$Ge$_{0.5}$ alloys show a more pronounced reduction in thermal conductivity (∼95% reduction compared to the thermal conductivity of crystalline Si), suggesting that compositional disorder has a larger impact on thermal conductivity reduction relative to structural disorder. It is also interesting to note that the minimum in thermal conductivity of the alloy is ∼18% lower than of a-Ge, while for crystalline systems, the minimum in thermal conductivity of the alloy can be as low as ∼92% compared to the thermal conductivity of crystalline Ge [50]. Moreover, in crystalline systems the minimum thermal conductivity is much lower than that of the parent materials; however, for the amorphous systems, the minimum is much closer to the a-Ge system.

In terms of the vibrational properties, the crystalline and amorphous phases of both silicon and germanium show similar bandwidths in their respective DOSs [11]. Figure 2(b) shows the vibrational DOS calculated from the Fourier transform of the velocity autocorrelation function (details of the calculation procedure are given in Refs. [51,52]) for a-Si, a-Ge, and a-Si$_{0.5}$Ge$_{0.5}$ domains. Similarly to crystalline alloys, the DOSs of the high-frequency vibrations are severely reduced while the DOSs for the low-frequency vibrations are increased in a-Si$_{0.5}$Ge$_{0.5}$ relative to that of a-Si.

For crystalline SiGe alloys, density functional theory calculations in Ref. [27] have shown that ∼87% of the heat is conducted by phonons below 2 THz. This enhanced low-frequency contribution has been attributed to the fact that higher-frequency vibrations are scattered due to lattice imperfections more so than low-frequency vibrations as the scattering rate is given by $\tau_{\text{imp}}^{-1} = A\omega^4$ with $A = \delta^3\Gamma/(4\pi v^3)$, where δ^3 is the atomic volume, v is the velocity, and Γ is the scattering cross section [53].

For alloys, the overall strength of scattering is determined by the mismatch in the host and the impurity atom's masses, the stiffness ratio between the host and the impurity atoms, and the impurity atom concentration. To investigate the influence of mass scattering on the thermal conductivity of a-Si$_x$Ge$_{1-x}$ alloys, we perform simulations on computational domains with silicon and germanium atoms described by the same interaction parameters for silicon alone and differentiated by only their mass mismatch. The thermal conductivity predictions for these systems are shown in Fig. 2(a) (hollow squares) along with those of a-Si$_x$Ge$_{1-x}$ alloys described by both mass mismatch and differences in Si-Si, Si-Ge, and Ge-Ge bonds. As is evident in the plot, the thermal conductivities of the mass-mismatched and the mass and bond mismatched systems demonstrate similar thermal conductivities and follow the same alloy-concentration trend. This suggests that the thermal conductivities of the alloys are mainly driven by mass-impurity scattering as opposed to any significant role from the bond disorder; this result might not be that surprising considering the fact that the radial distribution functions for silicon and germanium are almost identical [54]. Similar conclusions have been drawn experimentally for crystalline SiGe alloys [55,56] where the authors show good agreement between their thermal conductivity measurements via time-domain thermoreflectance and a theoretical model based on Klemen's perturbation theory [53],

which only considers reduction in thermal conductivity due to impurity-mass scattering. However, we note that for binary alloys with a relatively small mass ratio such as in PbTe and PbSe, the bond disorder has been shown to be relatively more important in comparison to the mass disorder while considering the strength of disorder-scattering in those alloys [57].

To investigate whether the disordered alloy marks the minimum achievable thermal conductivity in SiGe heterostructures, we run additional simulations on a-Si/a-Ge SL structures. Figure 2(c) shows the NEMD-predicted thermal conductivities for our a-Si/a-Ge SLs. In contrast to the a-Si, a-Ge, and a-Si_xGe_{1-x} alloys, the SLs do not show a statistically significant change in the predicted thermal conductivities for the different domain sizes as shown in Fig. 2(c). This can be attributed to the fact that the period thicknesses in the SLs are in the regime where propagons do not contribute significantly to heat conduction and the dominant heat carriers are diffusons; similar conclusions have been drawn for Stillinger-Weber based SLs of a-Si and mass-heavy Si in our previous work [11]. The monotonic decrease in thermal conductivity with increasing interface density suggests that with high interface densities, the thermal conductivity of these materials can be lowered below the theoretical minimum limit, which is generally attributed to the amorphous phases of materials where the "mean-free paths" of vibrations are limited to half the period spacing between the atoms [29]. In comparison to the thermal conductivity of the a-$Si_{0.5}Ge_{0.5}$ alloy [$\kappa_{Si_{0.5}Ge_{0.5}} = 0.77$ W m^{-1} K^{-1}, as shown by the dash-dotted line in Fig. 2(c)], the thermal conductivity of the SL structure can be lowered by as much as ~30% for an interface density of ~1.28 nm^{-1}.

Assuming that the NEMD-predicted thermal conductivities in each layer of the a-Si or a-Ge in the SLs are invariant with decreasing period thicknesses, we determine a resistance of $R_K = 0.72$ m^2 K GW^{-1} for a single a-Si/a-Ge interface. Recently, Gordiz and Henry have reported a resistance of 0.94 m^2 K GW^{-1} for an a-Si/a-Ge interface; however, this resistance also includes contributions from the scattering of propagating modes. They show that propagons contribute 54.7% of the total conductance across a-Si/a-Ge interfaces [58], whereas the resistance that we report is strictly due to delocalized and nonpropagating modes since our period thicknesses are much smaller than the wavelengths associated with propagating modes. As such, the resistance that we report is not the intrinsic resistance associated with an a-Si/a-Ge interface. We further note that the resistance reported in this work is assuming that the thermal conductivities of the layers do not vary with increasing interface densities; however, as we show in the following discussion, this approximation does not hold for SLs with small period thicknesses since the vibrational eigenmodes of the layers are severely affected by the inclusion of a-Si/a-Ge interfaces.

B. Diffusivities and participation ratios of individual eigenmodes

To investigate the effect of introducing Ge atoms and layers on the individual eigenmodes in a-SiGe alloys and a-Si/a-Ge SLs, respectively, we calculate the inverse participation ratio (IPR). To this effect, we perform lattice dynamics calculations to determine the eigenvectors of the vibrational modes. These

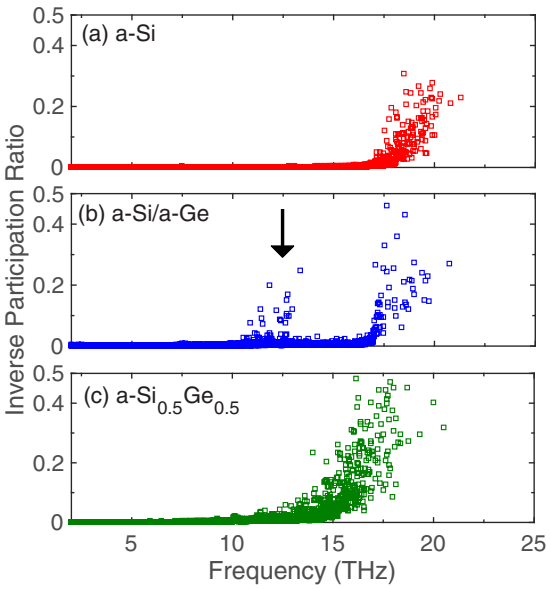

FIG. 3. Inverse participation ratios (IPRs) from lattice dynamics calculations for (a) a-Si, (b) a-Si/a-Ge with period thickness of 2.7 nm, and (c) a-$Si_{0.5}Ge_{0.5}$. In contrast to the IPRs for a-Si and a-$Si_{0.5}Ge_{0.5}$, the IPR for the a-Si/a-Ge structure shows a pronounced increase for modes at and around the cutoff frequency of the softer solid [arrow in (b)].

calculations are carried out with the General Utility Lattice Program (GULP) [59]. From the eigenvectors, we calculate the inverse participation ratio, which is defined as [6]

$$\frac{1}{p_n} = \sum_i \left[\sum_\alpha \epsilon_{i\alpha,n} \epsilon^*_{i\alpha,n} \right]^2, \tag{2}$$

where $\epsilon_{i\alpha,n}$ is the eigenvector component in the αth direction for mode n. If the vibrational mode is distributed equally over all the atoms, then the $\frac{1}{p_n}$ value would be $1/N$, whereas if the mode is localized on a single atom, the value would be 1. Therefore, $\frac{1}{p_n}$ measures the number of atoms vibrating with significant amplitude of the nth mode [6]. In other words, for delocalized modes $\frac{1}{p_n}$ tends to zero while for localized modes $\frac{1}{p_n}$ has a nonzero value.

Figures 3 shows the IPR calculated for a-Si (a), a-Si/a-Ge SL with a period thickness of 2.7 nm (b), and a-$Si_{0.5}Ge_{0.5}$ (c) structures. As mentioned above, delocalized modes have smaller IPR since they involve many atoms that vibrate collectively. However, locons are localized and involve very few atoms, and therefore exhibit larger IPR values. Consistent with prior works [6,49], the localized nature of vibrational eigenmodes in a-Si is observed for frequencies >16 THz [Fig. 3(a)]. For the SL structures, pronounced localized modes appear in the mid-frequency region between 10–13 THz as shown by the arrow in Fig. 3(b), which marks the cutoff frequency for the softer germanium layers [11], whereas in the case of a-$Si_{0.5}Ge_{0.5}$ [Fig. 3(c)], these modes show comparatively lower IPR values, while higher IPR values are observed for localized modes towards the latter end of the spectrum. This suggests

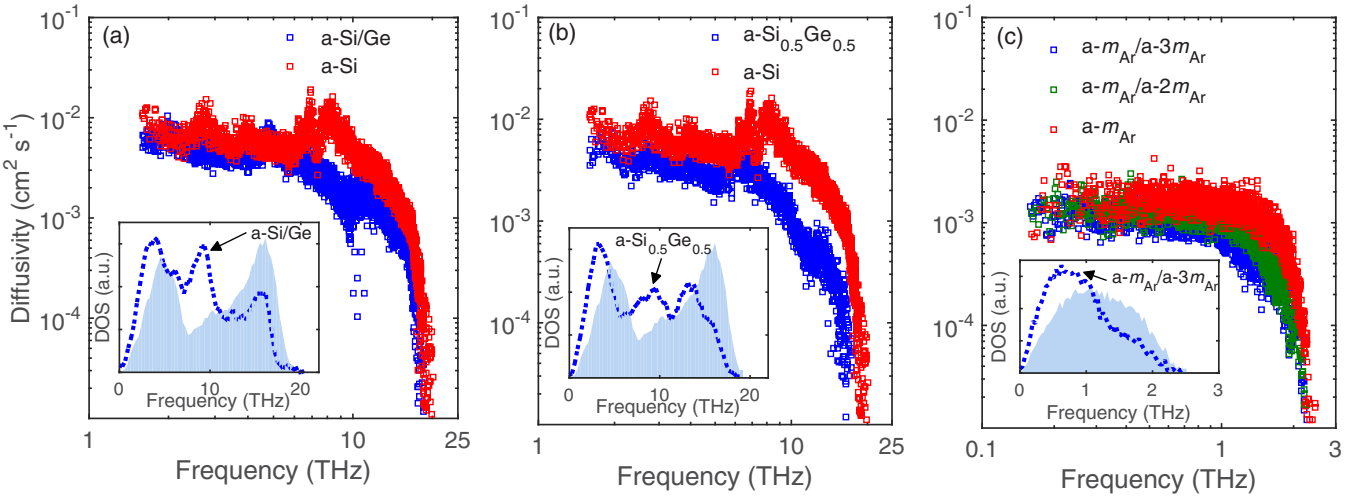

FIG. 4. Mode diffusivities calculations from the Allen and Feldman theory for (a) a-Si and a-Si/a-Ge structure, (b) a-Si and a-$Si_{0.5}Ge_{0.5}$, and (c) Lennard-Jones (LJ) argon, LJ-based superlattices with mass mismatch. In comparison to the diffusivities for a-Si and a-$Si_{0.5}Ge_{0.5}$, the diffusivities for a-Si/a-Ge structure show a pronounced decrease at 10 THz frequency due to the lower cutoff frequency of the softer germanium layer. However, this pronounced decrease is not observed in a-LJ-based superlattice structures. Insets: Density of states predicted via lattice dynamics calculations for (a) a-Si and a-Si/a-Ge structure, (b) a-$Si_{0.5}Ge_{0.5}$ along with the density of states for pure amorphous silicon, and (c) a-LJ Ar/mass-heavy a-LJ Ar along with density of states for pure a-LJ argon.

that the reduction in thermal conductivity observed for SL structures in Fig. 2(c) derives from the localized nature of vibrations in the 10–13 THz, while the reduction in thermal conductivity for the disordered alloys is mainly due to lower contributions to thermal conductivity from modes beyond the cutoff frequency of the softer solid in the binary alloy.

To show this more quantitatively, we calculate the thermal conductivity contributions based on the diffusivities of the eigenmodes in a-Si, a-Si/a-Ge, and a-$Si_{0.5}Ge_{0.5}$ structures. In this regard, to calculate the lower limit to the thermal conductivity contribution from each mode, we utilize the AF theory, which computes the contribution from diffusive and nonpropagating modes as [5,47]

$$\kappa_{\mathrm{AF}} = \sum_{\text{diffusons}} = \frac{k_{\mathrm{B}}}{V} D_{\mathrm{AF},n}(\omega_n), \tag{3}$$

where ω_n is the frequency of the nth diffuson and $D_{\mathrm{AF},n}$ under the harmonic approximation is calculated as

$$D_{\mathrm{AF},n}(\omega_n) = \frac{\pi V^2}{\hbar^2 \omega_n^2} \sum_{m \neq n} |S_{nm}|^2 \delta(\omega_n - \omega_m), \tag{4}$$

where $|S_{nm}|$ is the heat current operator for the harmonic modes. The Lorentzian broadening of the delta function must be several times greater than the average mode spacing, δ_{avg}. For our calculations, we set the broadening to $5\delta_{\mathrm{avg}}$ to satisfy this criteria; note, perturbing the Lorentzian broadening has negligible influence on the AF-predicted thermal conductivities (for example, changing the broadening by 20% changes the AF-predicted thermal conductivity for a-Si by ∼0.5%). Note that metastabilities in our relaxed structure result in imaginary frequencies, which have been neglected in our calculations and therefore do not affect the modal diffusivities. For a-Si,

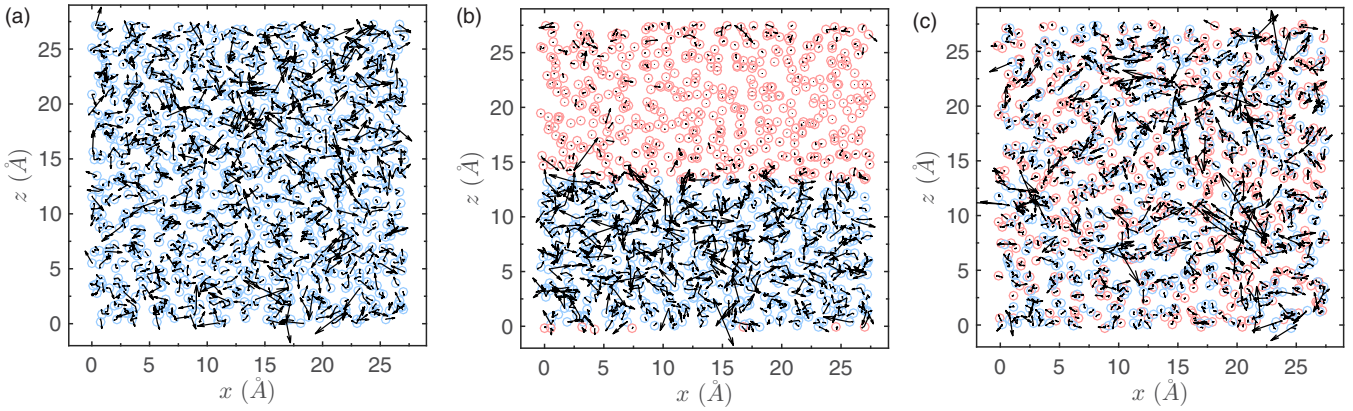

FIG. 5. Spatial components of the two-dimensional eigenvectors for 13.32 THz frequency modes in (a) a-Si, (b) a-Si/a-Ge, and (c) a-$Si_{0.5}Ge_{0.5}$ calculated via lattice dynamics calculations. The blue and red circles represent silicon and germanium atoms, respectively. In contrast to the spatial distribution of these modes throughout the a-Si and a-$Si_{0.5}Ge_{0.5}$ structures, these modes predominantly reside in the a-Si layer for the a-Si/a-Ge structure.

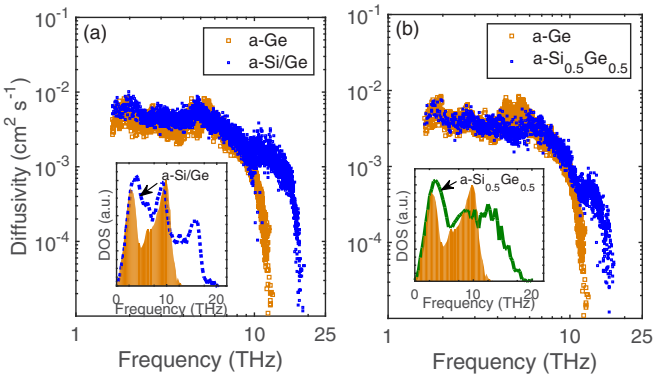

FIG. 6. Mode diffusivity calculations from the Allen and Feldman theory for (a) a-Ge and a-Si/a-Ge structure, (b) a-Ge and a-$Si_{0.5}Ge_{0.5}$. The diffusivities of the heterostructure are comparatively more similar to that of a-Ge than that in a-Si. Insets: Density of states predicted via lattice dynamics calculations for (a) a-Ge and a-Si/a-Ge structure, and (b) a-$Si_{0.5}Ge_{0.5}$ along with the density of states for pure amorphous germanium.

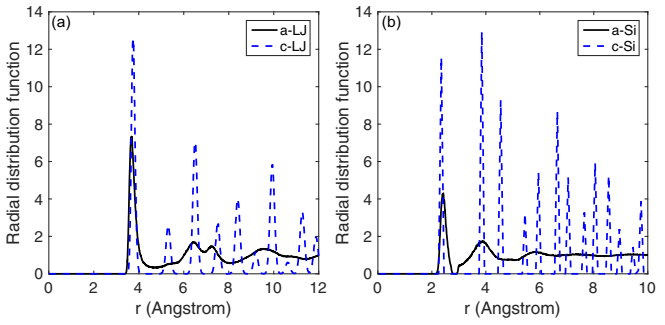

FIG. 7. Radial distribution functions (RDFs) for the crystalline and amorphous phases of (a) the Lennard-Jones argon and (b) Stillinger-Weber silicon systems. In contrast to that of the argon system, the second peak in the RDFs for silicon coincides for the amorphous and crystalline phases.

annealing for 10 ns at 1000 K results in 0.7% of the vibrational frequency that are imaginary, whereas an unannealed computational domain results in 1.5% of the vibrational frequency that are imaginary.

Figure 4 shows the spectral diffusivities for a-Si [Figs. 4(a) and 4(b); red squares], a-$Si_{0.5}Ge_{0.5}$ [Fig. 4(a); blue squares], and the a-Si/a-Ge SL [Fig. 4(b); blue squares]. While the diffusivity of modes <7 THz are similar for a-Si and the a-Si/a-Ge SLs, there is a large reduction in the diffusivity of ∼10 THz vibrations in the a-Si/a-Ge SL, which supports the findings from the IPR calculations. However, the diffusivities of modes <7 THz are similar for the two cases. This is in contrast to the results for a-$Si_{0.5}Ge_{0.5}$ as shown in Fig. 4(b) where the whole spectrum of frequencies in a-$Si_{0.5}Ge_{0.5}$ has lower diffusivities as compared to that in a-Si. The lower diffusivity around ∼10 THz in the SL structure compared to the alloy suggests that localization of these modes can result in comparatively lower thermal conductivities of the SL structures [see Fig. 2(a) and Fig. 2(c)]. Similar results have been shown for structures of amorphous SiGe nanocomposites with Ge clusters imbedded in a Si host matrix [48]. In the insets of Figs. 4(a) and 4(b), we show the DOS from the lattice dynamics calculations for a-Si/a-Ge and a-$Si_{0.5}Ge_{0.5}$ structures, respectively. As is clear, the DOS peak at the cutoff frequency of a-Ge is pronounced for the case of the layered structure, whereas most of the high-frequency modes in a-$Si_{0.5}Ge_{0.5}$ show reduced DOS due to alloy scattering. For comparison, we also calculate the diffusivities for our homogeneous a-Ge structure, which are shown in Fig. 6. The dip in diffusivities at ∼10 THz for the a-Si/a-Ge SL matches with the dip in diffusivities for the a-Ge structure (that is at and around the frequency cutoff for a-Ge). Also, the calculated diffusivities of modes for the a-$Si_{0.5}Ge_{0.5}$ structure is more similar to the modal diffusivities in a-Ge than in a-Si, which might explain the minimum in thermal conductivity of the alloy structures being comparatively closer to the thermal conductivity of a-Ge as shown in Fig. 2(a). Note that the DOSs calculated by taking the Fourier transform of the velocities in our MD simulations matches very well with the DOS from our lattice dynamics calculations, further solidifying our treatment of lattice dynamics to explain our MD results.

The results in Figs. 4(a) and 4(b) give rise to the question of whether the enhanced localization of modes in the SL structures at and around the cutoff frequency of the softer layer is applicable to any generic amorphous multilayers. To answer this question, we calculate the thermal diffusivities for Lennard-Jones (LJ) based amorphous multilayers (with LJ-Ar/heavy LJ-Ar structures). Figure 4(c) shows the diffusivity for amorphous LJ-Ar (red square) and multilayers of a-LJ-Ar and mass-heavy LJ-Ar. As expected, increasing the mass of the alternating layer from $2m_{Ar}$ to $3m_{Ar}$, the spectral diffusivities decrease. However, pronounced decrease in diffusivities at the cutoff frequency of the softer solid is not observed for these structures. This finding suggests that the mode localization for the a-Si/a-Ge SLs cannot be generalized for other amorphous multilayers. One reason for this phenomenon could potentially be due to the intrinsic differences in the DOSs for those of the silicon-based multilayers and that for the generic LJ-based multilayers. The inset of Fig. 4(c) shows the DOSs from

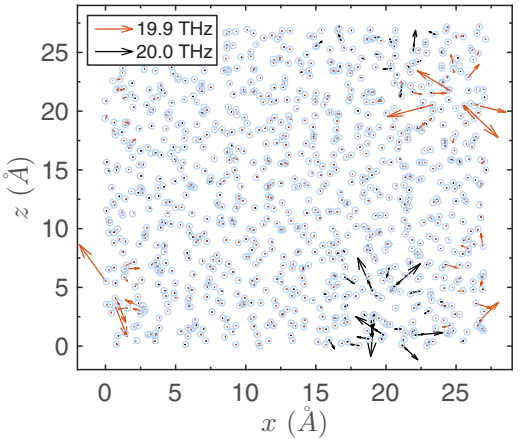

FIG. 8. Spatial components of the two-dimensional eigenvectors for 19.9 THz and 20.0 THz frequency modes in a-Si calculated via lattice dynamics calculations. The lack of spatial overlap between the eigenvectors of the modes suggests that these are locons.

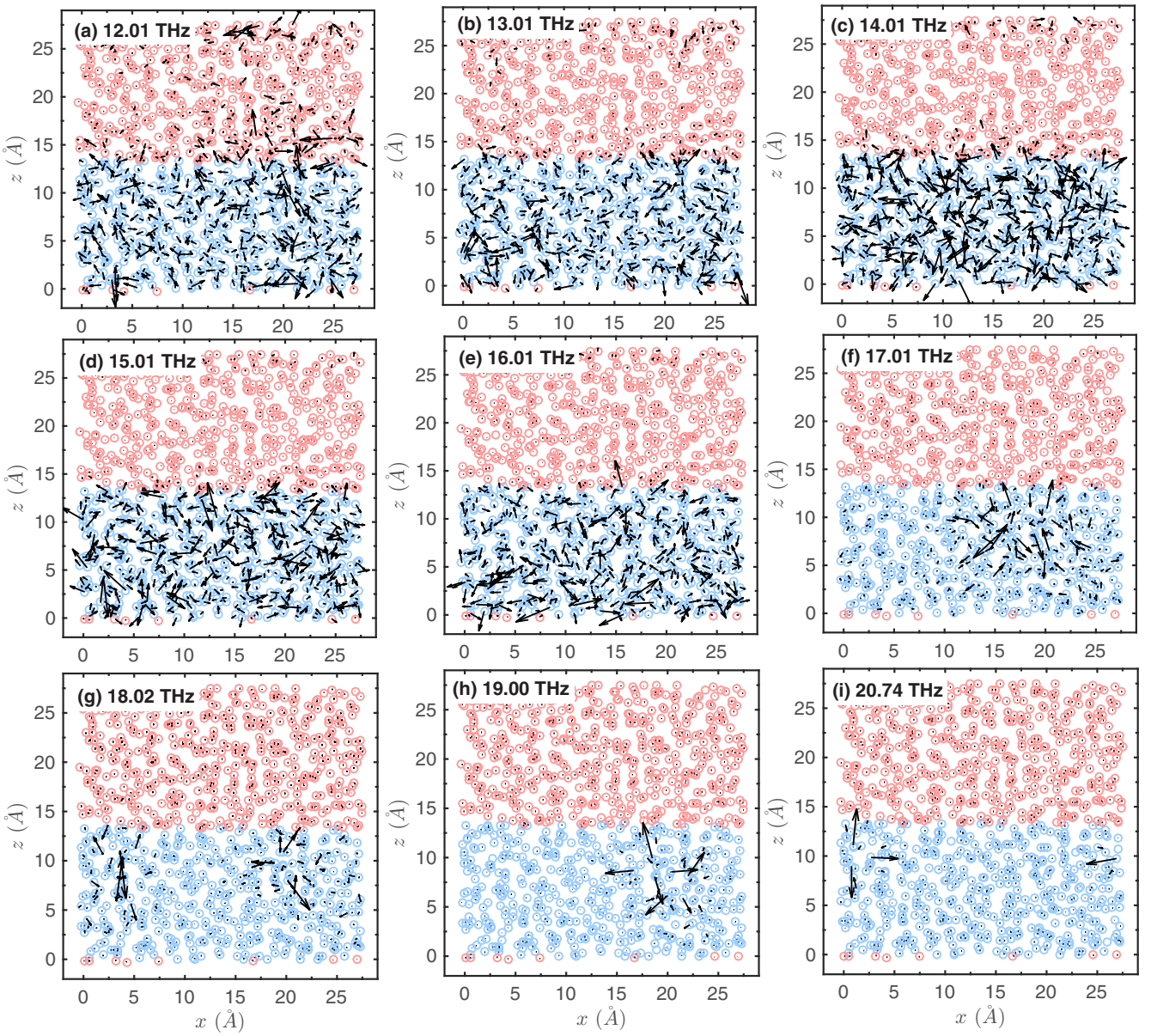

FIG. 9. Spatial components of the two-dimensional eigenvectors for a-Si/a-Ge structure in the 12–21 THz frequency range calculated via lattice dynamics calculations. The blue and red circles represent silicon and germanium atoms, respectively. These frequencies are above the cutoff frequency of the softer solid (germanium) and are therefore mostly confined to the a-Si layers.

the lattice dynamics calculations for amorphous LJ-Ar/heavy LJ-Ar structure where the heavier solid has three times the mass of LJ-Ar. The most apparent observation is that, contrary to the silicon-based structures, these LJ-based structures do not show a pronounced peak at the cutoff frequency of the softer solid (∼1.5 THz). Similar findings have been shown in Ref. [60] where large interfacial DOSs appear at the cutoff frequency of the softer side in silicon-based materials, whereas this large increase is not observed for the generic LJ-based interfaces. Another potential reason for the lack of pronounced mode localization at the cutoff frequency for LJ-based SLs might be due to the differences in their internal structure as compared to that of the silicon-based structures. The two structures possess varying radial distribution functions [9,46] (RDFs) signifying differing local environments (as shown in Fig. 7); while a-Si and a-Ge structures show a fourfold coordination on average, the intrinsic structure for LJ-based solids is composed of 12 nearest neighbors (as in their crystalline phase). Moreover, comparing the RDFs between the respective amorphous and crystalline phases of the two structures, the second peak in the RDF coincides for the SW-based solid, whereas the second peak for the amorphous phase in LJ-argon is further away as compared to that in the crystalline phase.

According to the AF theory, the diffusivity of the delocalized modes depends on the spatial overlap (i.e., how much the eigenvectors overlap) as well as the energetic overlap (i.e., how close the frequencies are to each other). For example, the eigenvectors of the two closest frequency modes in the a-Si are shown in Fig. 8; we only plot the two-dimensional (x and z components) of the eigenvectors for clarity. As is clear, the

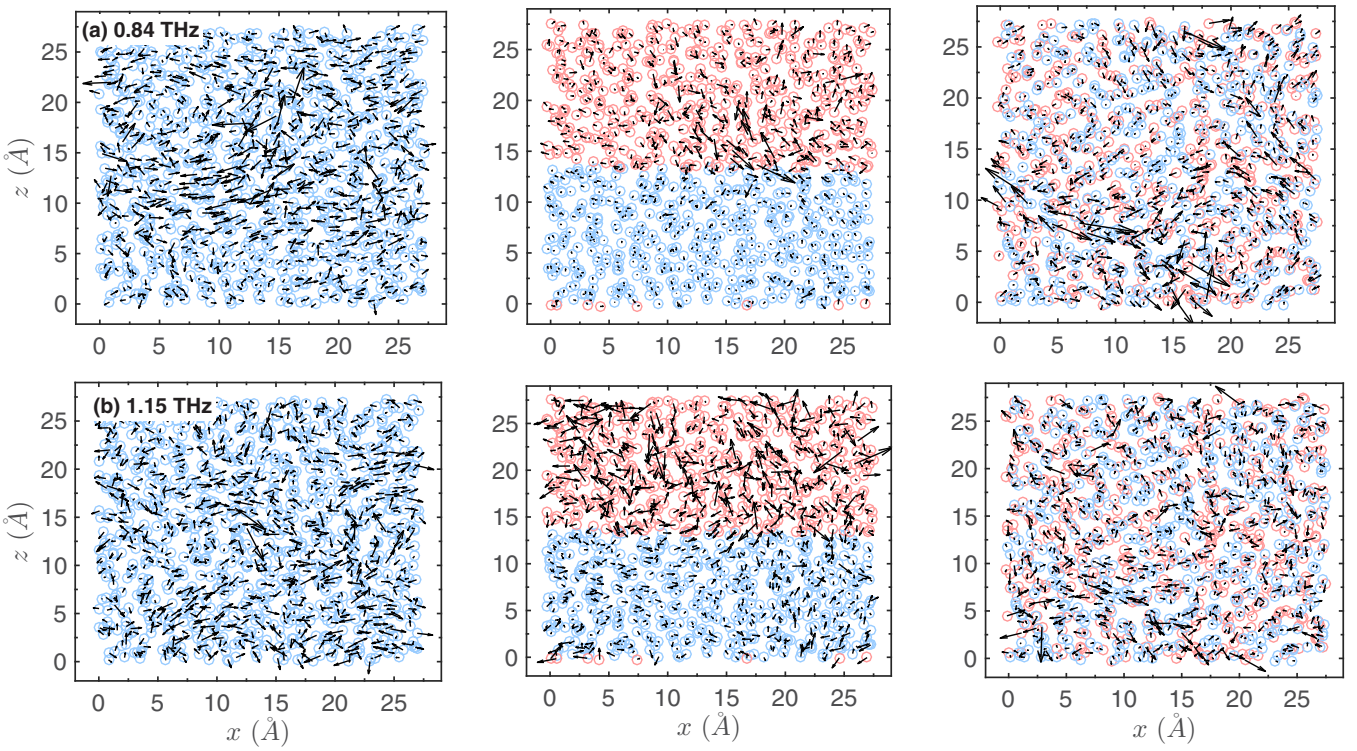

FIG. 10. Spatial components of the two-dimensional eigenvectors for (a) 0.84 THz and (b) 1.51 THz low-frequency modes in a-Si, a-Si/a-Ge, and a-$Si_{0.5}Ge_{0.5}$ structures. The blue and red circles represent silicon and germanium atoms, respectively. These low-frequency modes show preferred direction and similar magnitudes in their eigenvectors for a-Si and a-$Si_{0.5}Ge_{0.5}$ structures. However, layering in the a-Si/a-Ge structure disrupts this behavior.

spatial separation and localization of each of the two closest modes suggests that they are locons. Therefore, the lack of spatial overlap, even though these modes have very similar frequencies, prevents them from coupling with each other according to the AF theory. In this regard, the eigenvectors of the modes at and around the cutoff frequency of germanium predominantly reside in the silicon layers in the a-Si/a-Ge SLs. To demonstrate this, we plot the eigenvectors for 13.32 THz in a-Si, a-Si/a-Ge, and a-$Si_{0.5}Ge_{0.5}$ in Figs. 5(a), 5(b) and 5(c), respectively. The silicon atoms are represented by blue circles and the germanium atoms are represented by red circles. In the case of a-Si and a-$Si_{0.5}Ge_{0.5}$, these modes spread throughout the entire structure; however, for the the case of a-Si/a-Ge SLs, these modes primarily reside on the silicon layers. Therefore, the SL structures essentially limit the spatial overlap of delocalized modes over the entire amorphous structure, which in turn can lead to significantly reduced thermal conductivities even below the alloy limit as shown in Fig. 2(c). Furthermore, the eigenvectors of modes greater than the modes with the large reduction in diffusivities in the SL structure reside in the a-Si layers. This is clearly shown in Fig. 9 where we plot the two-dimensional eigenvectors for modes >11 THz in an interval of ~ 1 THz. This again points to the fact that layering can create a spatial separation for some of the eigenmodes, which cannot be achieved in the alloy structures as shown in Figs. 5(b) and 5(c) for the representative case of eigenvectors with 13.32 THz frequency.

For homogeneous a-Si, Self and Henry [61] have shown plane-wave-like character for modes below ~ 2 THz by quantitatively measuring the degree of spatial periodicity for each mode. Furthermore, they show that these modes do not exhibit clear randomness in the magnitude and direction of their eigenvectors despite the structural disorder. Indeed, both experimental and computational works have demonstrated that these propagating modes with plane-wave character contribute substantially to the thermal conductivity in homogeneous a-Si [62,63]. We do not attempt to separate the contributions from propagating and nonpropagating modes in this work and readers are referred to Refs. [10,61–63] for a rigorous treatment of this topic. However, to visualize the effect of layering on the velocity field of the propagating modes, we plot the eigenvectors for modes at 0.84 THz and 1.51 THz for a-Si, a-$Si_{0.5}Ge_{0.5}$, and a-Si/a-Ge in Fig. 10. These eigenmodes in a-Si and a-$Si_{0.5}Ge_{0.5}$ show similarity in their direction and magnitudes illustrating their propagating nature. However, for the a-Si/a-Ge structure, we observe that layering disrupts the motions of atoms that repeat spatially throughout the whole structure as signified by the lack of preferred direction or periodicity in the eigenvectors for the atoms.

The results and discussions presented in the preceding paragraphs demonstrate that in amorphous SiGe SLs, interfaces between amorphous silicon and amorphous germanium layers can be utilized to specifically lower the diffusivities and increase the localization of certain modes, which can lead to reduced thermal conductivities in the cross-plane direction. We utilize this approach to reducing the thermal conductivity in layered materials to amorphous SLs with three differing layers that demonstrate large reductions in diffusivities for certain eigenmodes in the phonon spectrum as described in the Appendix. Doing so leads to higher anisotropies

in thermal conductivity of silicon-based amorphous SL structures.

IV. CONCLUSIONS

We investigated the vibrational thermal transport mechanisms responsible for the reduced thermal conductivities in silicon and germanium heterostructures. Through NEMD simulations, we showed that pronounced size effects are apparent in a-Si, a-Ge, and a-SiGe alloys, whereas SL structures of the constituent materials leads to size-independent thermal conductivities. Contrary to their crystalline counterparts, we found that the GK-predicted and NEMD-predicted thermal conductivities of these materials are similar, which suggests that the minimum system sizes used in our NEMD simulations are comparable to or larger than the mean-free paths of the dominant heat-carrying vibrations in their respective systems. With respect to the thermal conductivity of amorphous silicon, amorphous $Si_{0.5}Ge_{0.5}$ demonstrates ∼53% reduction in thermal conductivity and our thermal conductivity predictions for a-Si/a-Ge SLs suggested that this alloy limit can be surpassed with interface densities above ∼0.35 nm^{-1}. By calculating the inverse participation ratios (IPRs) and diffusivities according to the AF theory for individual eigenmodes in the alloys and SLs, we attributed the larger reduction in thermal conductivity of SL structures in comparison to their disordered alloy counterparts to greater localization of modes at and around the cutoff frequency of the amorphous germanium layer.

ACKNOWLEDGMENTS

We appreciate support from the US Department of Defense, Office of Naval Research, Grant No. N00014-15-1-2769. A.G. is grateful to S. Pokharel for helpful discussions.

APPENDIX: LARGE ANISOTROPIES THROUGH LOCALIZATION OF EIGENMODES

We examine SL structures with three species of alternating layers of amorphous silicon, amorphous germanium, and mass-heavy amorphous silicon atoms with 5 times the mass of silicon (a-Si/a-Ge/a-h-Si) in an attempt to give rise to more localized modes in the frequency mode spectrum. We utilize equilibrium MD simulations under the GK formalism to predict the thermal conductivities of these SLs in the in-plane and cross-plane directions simultaneously. Figure 11(a) shows the GK-predicted thermal conductivities in the in-plane and cross-plane directions for the two-layer-period a-Si/a-Ge SLs (considering only mass mismatch) and for the three-layer-period a-Si/a-Ge/h-Si SLs as a function of interface density. Consistently with our previous NEMD results, the thermal conductivities monotonically decrease with increasing interface densities for the two SLs. As expected, the three-layered SL structures demonstrate lower thermal conductivities compared to the two-layered SLs due to the inclusion of the relatively softer and heavier layer (with $m_{h-Si} = 5m_{Si}$). Along with the cross-plane thermal conductivities, we also plot the in-plane thermal conductivity predictions for these structures. Note that the reduction in thermal conductivity with interface density is not so obvious in the in-plane direction.

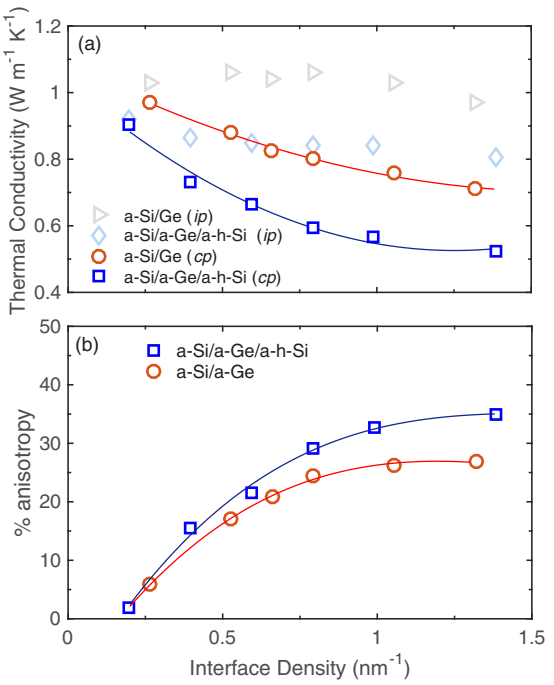

FIG. 11. (a) GK-predicted thermal conductivities of the three-layered a-Si/a-Ge/h-Si SLs and the two-layered a-Si/a-Ge SLs as a function of interface. Both the cross-plane and in-plane components of the thermal conductivity for these structures are shown for comparison. (b) Comparison between the anisotropy in the in-plane (ip) and cross-plane (cp) thermal conductivities for the two-layered and three-layered SLs as a function of interface densities. The lines are to guide the eye.

In Fig. 11(b) we plot the percentage of anisotropy defined as $(\kappa_{ip} - \kappa_{cp})/\kappa_{ip} \times 100\%$, between the in-plane and cross-plane thermal conductivities for the two- and three-layered SLs. At moderate interface densities, both the structures show similar anisotropic increase in thermal conductivity; however, at higher interface densities, the three-layered structures demonstrate significantly higher thermal anisotropies—up to 35% in anisotropy in thermal conductivity is observed for three-layered SLs as compared to ∼26% in two-layered SLs. This suggests that the three-layered structures are better in reducing the relative thermal conductivities in the cross-plane direction as compared to the in-plane direction.

The pronounced localized modes associated with SiGe interfaces at the cutoff frequency of Ge appears at lower frequency modes for the a-Si/a-Ge/a-h-Si structures due to the relatively lower cutoff frequency of the softer a-h-Si layers as highlighted in Fig. 12(a), which shows our IPR calculations for the three-layered structure. We also calculate the diffusivities of the three-layered structure in Fig. 12(b) (green squares) where we compare the calculations with that for the two-layered a-Si/a-Ge structure (pink squares). As is evident, the diffusivities of the entire spectrum of modes are drastically reduced due to the inclusion of the heavier h-Si layers. Consistently with the two-layered structures, the diffusivities of the modes at and around the cutoff frequencies of the softer solids are reduced significantly. The inclusion of the a-h-Si layer also leads to the localization of modes between

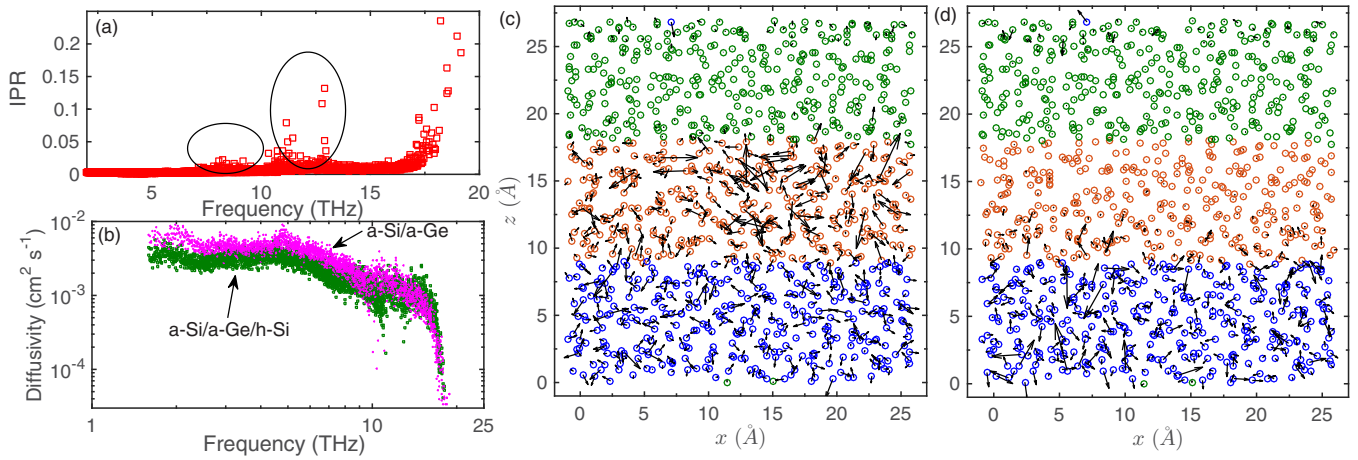

FIG. 12. (a) Spectral IPR for the three-layered a-Si/a-Ge/a-h-Si structure showing the pronounced localization of modes at and near the cutoff frequencies of the softer solids. (b) Comparison of mode diffusivities between the two-layered a-Si/a-Ge and three-layered a-Si/a-Ge/a-h-Si structures as predicted via Eq. (4). Spatial components of the two-dimensional eigenvectors for (c) 10.63 THz and (d) 12.05 THz modes for the three-layered system. The blue, red, and green circles represent silicon, germanium, and 5×heavy-silicon atoms, respectively.

the cutoff frequency of a-h-Si and germanium as shown by the two-dimensional plot of the eigenvectors for the a-Si/a-Ge/a-h-Si system in Fig. 12(b) for a 10.63 THz frequency mode. These modes reside predominantly in the silicon and germanium layers. Furthermore, similarly to the two-layered structures, the modes greater than the cutoff frequency of germanium reside in the silicon layers as shown by the eigenvectors for the 12.05 THz eigenmode in Fig. 12(c).

[1] C. Kittel, *Introduction to Solid State Physics*, 6th ed. (John Wiley & Sons, Inc., New York, 1986).

[2] P. G. Klemens, Thermal Conductivity and Lattice Vibrational Modes, *Solid State Physics* (Academic Press, 1958), pp. 1–98.

[3] K. Esfarjani, G. Chen, and H. T. Stokes, Phys. Rev. B **84**, 085204 (2011).

[4] D. A. Broido, M. Malorny, G. Birner, N. Mingo, and D. A. Stewart, Appl. Phys. Lett. **91**, 231922 (2007).

[5] P. B. Allen and J. L. Feldman, Phys. Rev. B **48**, 12581 (1993).

[6] J. L. Feldman, M. D. Kluge, P. B. Allen, and F. Wooten, Phys. Rev. B **48**, 12589 (1993).

[7] P. B. Allen and J. L. Feldman, Phys. Rev. Lett. **62**, 645 (1989).

[8] P. B. Allen, J. L. Feldman, J. Fabian, and F. Wooten, Philos. Mag. B **79**, 1715 (1999).

[9] J. M. Larkin and A. J. H. McGaughey, Phys. Rev. B **89**, 144303 (2014).

[10] J. L. Braun, C. H. Baker, A. Giri, M. Elahi, K. Artyushkova, T. E. Beechem, P. M. Norris, Z. C. Leseman, J. T. Gaskins, and P. E. Hopkins, Phys. Rev. B **93**, 140201 (2016).

[11] A. Giri, P. E. Hopkins, J. G. Wessel, and J. C. Duda, J. Appl. Phys. **118**, 165303 (2015).

[12] S. Kwon, J. Zheng, M. C. Wingert, S. Cui, and R. Chen, ACS Nano **11**, 2470 (2017).

[13] E. T. Swartz and R. O. Pohl, Rev. Mod. Phys. **61**, 605 (1989).

[14] P. E. Hopkins, ISRN Mech. Eng. **2013**, 682586 (2013).

[15] S.-M. Lee, D. G. Cahill, and R. Venkatasubramanian, Appl. Phys. Lett. **70**, 2957 (1997).

[16] W. S. Capinski, H. J. Maris, T. Ruf, M. Cardona, K. Ploog, and D. S. Katzer, Phys. Rev. B **59**, 8105 (1999).

[17] T. Borca-Tasciuc, W. Liu, J. Liu, T. Zeng, D. W. Song, C. D. Moore, G. Chen, K. L. Wang, M. S. Goorsky, T. Radetic, R. Gronsky, T. Koga, and M. S. Dresselhaus, Superlattices Microstruct. **28**, 199 (2000).

[18] M. N. Touzelbaev, P. Zhou, R. Venkatasubramanian, and K. E. Goodson, J. Appl. Phys. **90**, 763 (2001).

[19] E. S. Landry, M. I. Hussein, and A. J. H. McGaughey, Phys. Rev. B **77**, 184302 (2008).

[20] Y. K. Koh, Y. Cao, D. G. Cahill, and D. Jena, Adv. Funct. Mater. **19**, 610 (2009).

[21] M. N. Luckyanova, J. Garg, K. Esfarjani, A. Jandl, M. T. Bulsara, A. J. Schmidt, A. J. Minnich, S. Chen, M. S. Dresselhaus, Z. Ren, E. A. Fitzgerald, and G. Chen, Science **338**, 936 (2012).

[22] R. Venkatasubramanian, Phys. Rev. B **61**, 3091 (2000).

[23] Y. Wang, C. Liebig, X. Xu, and R. Venkatasubramanian, Appl. Phys. Lett. **97**, 083103 (2010).

[24] J. Ravichandran, A. K. Yadav, R. Cheaito, P. B. Rossen, A. Soukiassian, S. J. Suresha, J. C. Duda, B. M. Foley, C.-H. Lee, Y. Zhu, A. W. Lichtenberger, J. E. Moore, D. A. Muller, D. G. Schlom, P. E. Hopkins, A. Majumdar, R. Ramesh, and M. A. Zurbuchen, Nat. Mater. **13**, 168 (2014).

[25] A. Giri, J. L. Braun, J. A. Tomko, and P. E. Hopkins, Appl. Phys. Lett. **110**, 233112 (2017).

[26] R. Cheaito, J. C. Duda, T. E. Beechem, K. Hattar, J. F. Ihlefeld, D. L. Medlin, M. A. Rodriguez, M. J. Campion, E. S. Piekos, and P. E. Hopkins, Phys. Rev. Lett. **109**, 195901 (2012).

[27] J. Garg, N. Bonini, B. Kozinsky, and N. Marzari, Phys. Rev. Lett. **106**, 045901 (2011).

[28] A. Einstein, Ann. Phys. **340**, 898 (1911).

[29] D. G. Cahill, S. K. Watson, and R. O. Pohl, Phys. Rev. B **46**, 6131 (1992).

[30] S. Shenogin, A. Bodapati, P. Keblinski, and A. J. H. McGaughey, J. Appl. Phys. **105**, 034906 (2009).
[31] D. G. Cahill and R. O. Pohl, Phys. Rev. B **35**, 4067 (1987).
[32] F. H. Stillinger and T. A. Weber, Phys. Rev. B **31**, 5262 (1985).
[33] M. Laradji, D. P. Landau, and B. Dünweg, Phys. Rev. B **51**, 4894 (1995).
[34] D. P. Sellan, E. S. Landry, J. E. Turney, A. J. H. McGaughey, and C. H. Amon, Phys. Rev. B **81**, 214305 (2010).
[35] M. Ishimaru, S. Munetoh, and T. Motooka, Phys. Rev. B **56**, 15133 (1997).
[36] S. Plimpton, J. Comput. Phys. **117**, 1 (1995).
[37] J. L. Feldman, P. B. Allen, and S. R. Bickham, Phys. Rev. B **59**, 3551 (1999).
[38] P. K. Schelling, S. R. Phillpot, and P. Keblinski, Phys. Rev. B **65**, 144306 (2002).
[39] C. Oligschleger and J. C. Schön, Phys. Rev. B **59**, 4125 (1999).
[40] L. Chen, X. Wang, and S. Kumar, Sci. Rep. **5**, 12763 (2015).
[41] Y. Chen, D. Li, J. R. Lukes, Z. Ni, and M. Chen, Phys. Rev. B **72**, 174302 (2005).
[42] Y. He, D. Donadio, and G. Galli, Appl. Phys. Lett. **98**, 144101 (2011).
[43] M. P. Allen and D. J. Tildesley, *Computer Simulation of Liquids*, reprint ed., Oxford Science Publications (Oxford University Press, New York, 1989).
[44] A. McGaughey and M. Kaviany, Int. J. Heat Mass Transf. **47**, 1783 (2004).
[45] A. McGaughey and M. Kaviany, Int. J. Heat Mass Transf. **47**, 1799 (2004).
[46] A. J. H. McGaughey, Phonon transport in molecular dynamics simulations: Formulation and thermal conductivity prediction, Ph.D. thesis, University of Michigan, 2004.
[47] J. M. Larkin and A. J. H. McGaughey, J. Appl. Phys. **114**, 023507 (2013).
[48] J. Moon and A. J. Minnich, RSC Adv. **6**, 105154 (2016).
[49] W. Lv and A. Henry, New J. Phys. **18**, 013028 (2016).
[50] T. Hori, T. Shiga, and J. Shiomi, J. Appl. Phys. **113**, 203514 (2013).
[51] J. C. Duda, T. S. English, E. S. Piekos, W. A. Soffa, L. V. Zhigilei, and P. E. Hopkins, Phys. Rev. B **84**, 193301 (2011).
[52] A. Giri and P. E. Hopkins, Appl. Phys. Lett. **105**, 033106 (2014).
[53] P. G. Klemens, Proc. Phys. Soc., London, Sect. A **68**, 1113 (1955).
[54] F. Alvarez, C. C. Díaz, A. A. Valladares, and R. M. Valladares, Phys. Rev. B **65**, 113108 (2002).
[55] D. G. Cahill, F. Watanabe, A. Rockett, and C. B. Vining, Phys. Rev. B **71**, 235202 (2005).
[56] D. G. Cahill and F. Watanabe, Phys. Rev. B **70**, 235322 (2004).
[57] T. Murakami, T. Shiga, T. Hori, K. Esfarjani, and J. Shiomi, Europhys. Lett. **102**, 46002 (2013).
[58] K. Gordiz and A. Henry, J. Appl. Phys. **121**, 025102 (2017).
[59] J. D. Gale and A. L. Rohl, Mol. Simul. **29**, 291 (2003).
[60] A. Giri and P. E. Hopkins, Sci. Rep. **7**, 11011 (2017).
[61] H. R. Seyf and A. Henry, J. Appl. Phys. **120**, 025101 (2016).
[62] K. T. Regner, D. P. Sellan, Z. Su, C. H. Amon, A. J. H. McGaughey, and J. A. Malen, Nat. Commun. **4**, 1640 (2013).
[63] J. Moon, B. Latour, and A. J. Minnich, Phys. Rev. B **97**, 024201 (2018).